Simple and Versatile Pharmacokinetic Model for Radioligand Therapy

Adrian Jun Zounek[1], Alexis Nikolai Zounek

[1] Department of Nuclear Medicine, University Hospital, LMU Munich

Correspondence: adrian.zounek@med.uni-muenchen.de

Abstract: In recent years radioligand therapy has emerged as an effective treatment modality for various solid malignancies, with pharmacokinetic modeling being routinely used for absorbed dose calculation and patient-specific therapy planning. Exemplary time-activity curves of FAP-targeted radioligands in a mouse model are accurately fitted by a sum of right skew biexponential distributions with four adjustable parameters in total. This type of modeling function is versatile and also suitable for conventional drugs. For further insight, an auxiliary equation is derived that relates tumor clearance to FAP expression and the radioligand dissociation constant.

Radioligand therapy (RLT) has been recognized as a promising treatment modality for solid tumors as demonstrated by the March 2022 FDA approval of [^{177}Lu]-PSMA-617 (Pluvicto®, Novartis AG, Basel, Switzerland) for the treatment of metastatic castration-resistant prostate cancer (mCRPC). Worldwide efforts are underway to develop new radioligands and expand the scope of RLT. In order to support these efforts and to gain a better understanding of RLT, various physiologically based pharmacokinetic (PBPK) models have been devised and adopted for patient-specific dosimetry and therapy planning. Despite their high utility PBPK models often include a large number of adjustable parameters with limited interpretability.

In this article, a simple and versatile PBPK model with only four adjustable parameters is presented. The model requires a blood time-activity curve (TAC), which can be obtained based on image data or using automatic or manual blood sampling. The two main parameters of the PBPK model refer to two exponential rate constants, which are similar to the eigenvalues of a multi-compartment model.

An N-compartment model includes 2N-1 micro or tissue rate constants and has N eigenvalues and N amplitudes for each compartment (N^2 amplitudes total). The model eigenvalues and amplitudes of each compartment may be determined from the corresponding time-activity or time-concentration curves via nonlinear regression. However, this approach often proves to be problematic due to overfitting and leads to inaccurate results - especially for small eigenvalues, i.e. slow processes.

The proposed PBPK model uses a simple and numerically stable regression method to determine the eigenvalues and amplitudes based on the TACs of the blood and tumor

compartment. The TAC of the tumor compartment is fitted with functions of type $\frac{e^{-\kappa \cdot t} - e^{-\beta \cdot t}}{\beta - \kappa}$, which corresponds to a right skewed biexponential distribution [1].

For therapeutic use, the primary goal is to describe the TAC of the tumor compartment with high reliability. Knowledge of tissue rate constants is of great interest for basic understanding but is not clinically required.

The article further presents a formula that describes radioligand clearance from tumor tissue by a simple function of affinity, target receptor concentration and "regular" pharmacokinetic clearance without receptor interference. To the best of our knowledge, this is the first time such a relationship has been derived.

RLT uses radioligands that preferentially accumulate in tumor tissue and expose them to an elevated radiation dose. Radioligand compounds comprise a targeting moiety or ligand coupled to a chelator via a spacer. The ligand binds to a biological receptor, such as prostate specific membrane antigen (PSMA), fibroblast activation protein (FAP) or a somatostatin receptor (SSTR) that is overexpressed in neoplastic lesions. The ligand can be a monoclonal antibody, a peptide or a small peptidomimetic molecule. The chelator is suited for complexation of a diagnostic or therapeutic radioisotope, such as ^{68}Ga, ^{177}Lu, ^{90}Y, ^{225}Ac having a half-life of 68 min, 6.65 d, 64.1 h and 9.92 d, respectively. Depending on the radioisotope the ionizing radiation dose is delivered primarily by high-energy photons, electrons or alpha-particles. The spacer couples the chelator and therewith complexed radioisotope to the targeting ligand while at the same time mitigating the interference of the chelator with ligand binding to its target receptor.

RLT uses radioligands with rapid systemic excretion and, conversely, high uptake and long retention in tumor tissue. For the latter, the affinity of the radioligand to its target receptor plays a crucial role. Affinity is quantified by its reciprocal, the dissociation constant K_D, preferably in units of nM (10^{-9} mol·L^{-1}). For the clinically approved radiotracer [^{177}Lu]-PSMA-617, Wen et al. [2] report values of K_D = 4.7 nM and k_{off} = 3.44 × 10^{-4} s^{-1}. k_{off} denotes the equilibrium dissociation rate, which in the case of [^{177}Lu]-PSMA-617 corresponds to a binding half-life of ln(2)/3.44 × 10^4 s = 33.6 min. The latter is 285 times smaller than the 9751.0 min (6.65 d) half-life of the therapeutic radioisotope ^{177}Lu. The large difference between the binding half-life of radioligands and therapeutic radioisotopes used for them is remarkable and deserves explanation. Due to 90 % cellular internalization [^{177}Lu]-PSMA-617 has a retention half-life in tumor tissue in the range from 68,0 h to 74,5 h which exceeds its binding half-life by a factor of about 127 (cf. Galler et al. [3], Fig. 8 legend). However, for radioligands that bind to FAP-positive CAFs, the internalization ratio appears to be considerably lower [4, 5]. Accordingly, the retention time in tumor tissue is largely limited by radioligand dissociation from extracellular FAP.

Without cellular internalization, retention in tumor tissue depends on radioligand pharmacokinetics and K_D or affinity to the target receptor R. As shown in appendix A, the

rate constant κ_e for radioligand clearance from tumor tissue is linked to the dissociation constant K_D and the intratumoral receptor concentration $[R]_t$ via the following relationship:

$$\kappa_e = \kappa_{PK} \frac{K_D}{K_D + [R]_t} \qquad (I)$$

wherein κ_{PK} denotes the physiological clearance rate in the absence of the target receptor R. According to equation (I) κ_e tends towards κ_{PK} for large dissociation constant $K_D \gg [R]_t$ i.e. low affinity. If κ_{PK}, K_D and $[R]_t$ are known, equation (I) can be used to calculate κ_e. Conversely, the intratumoral receptor concentration $[R]_t$ may be determined based on κ_e, κ_{PK} and K_D.

The physiological clearance rate κ_{PK} in tumor tissue largely depends on intercellular diffusion and convection. Convection can be accelerated due to fenestrated vasculature or shunts between arterial and venous capillaries, as commonly found in tumor tissue. In contrast to normal tissue, lymphatic clearance in tumor tissue is severely impaired. Regardless of the different physiology of tumor and normal tissue, the latter can serve as a useful approximation for κ_{PK}. Alternatively, κ_{PK} can be experimentally determined using multilayered cell cultures or multicellular spheroids.

As can be gathered from equation (I) the effective clearance rate κ_e can be lowered by reducing either κ_{PK} or K_D. Modification of radioligand chemistry affects both κ_{PK} and K_D. Therefore, it may be difficult to distinguish or decouple the effect of reduced K_D from the effect of altered κ_{PK} in tumor tissue and pharmacokinetics in healthy tissue. This interdependence must be heeded especially if clearance from other tissues such as liver or bone marrow is slow.

Reducing κ_{PK} is likely to prolong radioligand retention in healthy tissue, which is generally undesirable. Notwithstanding, strategies aimed at prolonging retention in the blood compartment can improve efficacy, as recently shown using radioligands equipped with an additional albumin binding moiety [6-9].

The proposed PBPK model is based on the familiar differential equation (II)

$$\frac{d[L]_t}{dt} = -\kappa_e \cdot [L]_t + \kappa_i \cdot [L]_b \qquad (II)$$

comprising a source term $\kappa_i \cdot [L]_b$ and a clearance term $-\kappa_e \cdot [L]_t$ wherein the source term is the product of the radioligand uptake rate κ_i times the concentration $[L]_b$ in blood. Clearance is likewise described by the product of the clearance rate κ_e times the intratumoral concentration $[L]_t$. Integration of equation (II) yields the general solution:

$$[L]_t = C \frac{1}{\kappa_e} e^{-\kappa_e \cdot t} + \kappa_i \int [L]_b \, dt \qquad (III)$$

If $[L]_b$ can be represented by a single exponential function of type

$$[L]_b = Be^{-\beta \cdot t} \qquad (IV)$$

the solution of equation (III) takes the form:

$$[L]_t = [L]_{t0}\, e^{-\kappa_e \cdot t} + \frac{\kappa_i\, B}{\beta - \kappa_e}\left(e^{-\kappa_e \cdot t} - e^{-\beta \cdot t}\right) \qquad (V)$$

wherein the initial tumor ligand activity $[L]_{t0}$ is equal to zero in most cases and the term $\frac{\kappa_i\, B}{\beta - \kappa_e}\left(e^{-\kappa_e \cdot t} - e^{-\beta \cdot t}\right)$ corresponds to a right skewed biexponential distribution [1].

The solution according to equation (V) tacitly ignores radioligand clearance from tumor tissue into the venous blood compartment and may violate mass conservation. However, this neglect is justified for clinical patients in whom tumor lesions typically constitute a small portion of body mass. Furthermore, as the beneath examples show, a model with two terms of type $\frac{\kappa_i\, B}{\beta - \kappa_e}\left(e^{-\kappa_e \cdot t} - e^{-\beta \cdot t}\right)$ and four adjustable parameters can describe tumor TACs in mouse xenografts despite abnormally large tumor-to-body mass ratios.

Taking mass conservation into account, on the other hand, requires a multi-compartment model with four or more compartments and numerical solution of a corresponding system of coupled differential equations with seven or more adjustable parameters. Apart from notoriously unstable numerical solutions and overfitting, an increase in the number of adjustable parameters makes meaningful interpretation difficult.

To demonstrate the use and versatility of the proposed PBPK model, two terms of the type $\frac{\kappa_i\, B}{\beta - \kappa_e}\left(e^{-\kappa_e \cdot t} - e^{-\beta \cdot t}\right)$ were used to fit experimental TACs measured by Wang et al. in mouse xenograft models for four different FAP radioligands [10]. In addition to the well-known reference compound FAPI-04, Wang et al. report experimental TACs for three newly designed radioligands denoted as "Ga-3-3", "Ga-6-3" and "Ga-8-1". For a detailed description of the latter the reader is referred to their article.

Growing evidence supports the notion that FAP-expressing cancer associated fibroblasts (CAF^{FAP+}) suppress anti-cancer immune response and promote tumor progression and metastasis [11]. Accordingly, FAP constitutes a promising target receptor for chemotherapy and RLT. Recent clinical results indicate that FAP-targeted RLT can be an effective and benign treatment modality [12-14].

The systematic study by Wang et al. can provide valuable clues for improving FAP-targeted radioligands. Their experimental data highlight the quite variable effects of radioligand pharmacokinetics on TACs and tumor dose, making validation of a PBPK model challenging. For these reasons, their data was chosen to test the proposed PBPK model.

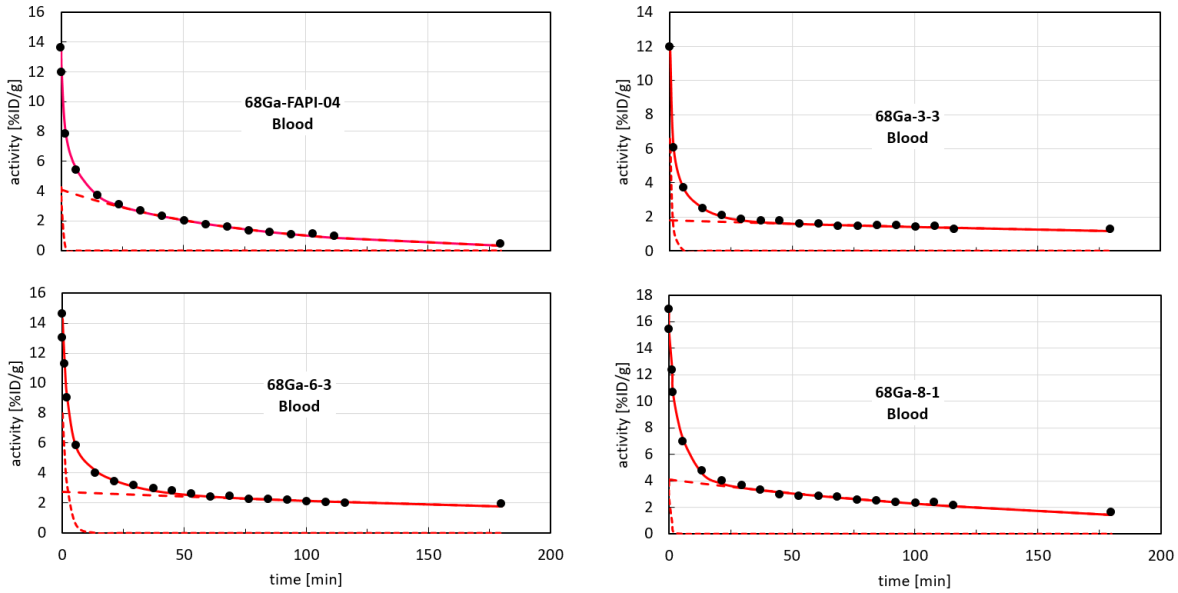

- Data from Wang et al. —— Triexponential fit ------ $B_1 \exp(-\beta_1 \cdot t)$ - - - $B_3 \exp(-\beta_3 \cdot t)$

Fig. 1: Blood TACs fitted to the data measured by Wang et al. [10].

	B_1 [%ID/g]	β_1 [min^{-1}]	B_2 [%ID/g]	β_2 [min^{-1}]	B_3 [%ID/g]	β_3 [min^{-1}]	$\sqrt{(\chi^2)}$ [%ID/g]	AUC_b [%ID g^{-1} min]
FAPI-04	4.27	1.926	5.26	0.1781	4.09	0.0139	0.06	326.5
Ga-3-3	9.23	1.136	3.68	0.1132	1.80	0.0023	0.06	819.6
Ga-6-3	8.14	0.491	3.59	0.0631	2.72	0.0023	0.13	1239.7
Ga-8-1	4.24	1.713	8.91	0.1791	4.09	0.0057	0.14	767.2

Table 1: Fit parameters of the blood TACs.

First the blood and tumor TACs of Fig. 5b of Wang et al. for radioligands FAPI-04, Ga-3-3, Ga-6-3 and Ga-8-1 were digitized. Each of the four digitized blood TACs was then fitted by a triexponential function of type:

$$[L]_b = B_1 e^{-\beta_1 \cdot t} + B_2 e^{-\beta_2 \cdot t} + B_3 e^{-\beta_3 \cdot t} \qquad (VI)$$

The fitted model curves and corresponding parameter values are presented in Fig. 1 and Table 1. Integration of equation (VI) yields the area under the curve for the blood concentration $[L]_b$ as

$$AUC_b = \int_0^\infty [L]_b \, dt = \frac{B_1}{\beta_1} + \frac{B_2}{\beta_2} + \frac{B_3}{\beta_3} \qquad (VIa)$$

The function used to fit the tumor TACs is represented by the following formula (VII):

$$\begin{aligned}[L]_t = \frac{\rho}{\rho+1}\Bigg[&[L]_{t0}\, e^{-\kappa_f \cdot t} + \frac{\kappa_i\, B_1}{\beta_1 - \kappa_f}\left(e^{-\kappa_f \cdot t} - e^{-\beta_1 \cdot t}\right) + \frac{\kappa_i\, B_2}{\beta_2 - \kappa_f}\left(e^{-\kappa_f \cdot t} - e^{-\beta_2 \cdot t}\right) \\ &+ \frac{\kappa_i\, B_3}{\beta_3 - \kappa_f}\left(e^{-\kappa_f \cdot t} - e^{-\beta_3 \cdot t}\right)\Bigg] \\ &+ \frac{1}{\rho+1}\Bigg[[L]_{t0}\, e^{-\kappa_s \cdot t} + \frac{\kappa_i\, B_1}{\beta_1 - \kappa_s}\left(e^{-\kappa_s \cdot t} - e^{-\beta_1 \cdot t}\right) + \frac{\kappa_i\, B_2}{\beta_2 - \kappa_s}\left(e^{-\kappa_s \cdot t} - e^{-\beta_2 \cdot t}\right) \\ &+ \frac{\kappa_i\, B_3}{\beta_3 - \kappa_s}\left(e^{-\kappa_s \cdot t} - e^{-\beta_3 \cdot t}\right)\Bigg] \qquad (VII)\end{aligned}$$

comprising exponential terms according to equation (V) and four adjustable parameters κ_i , κ_f , κ_s , ρ . The exponential rate constants κ_f , κ_s , β_1 , β_2 , β_3 are similar to the eigenvalues of a 5-compartment model and do not directly correspond to physiological tissue rate constants, but rather are complicated functions thereof. As can be easily shown through differentiation, the intratumoral radioligand activity $[L]_t$ of equation (VII) satisfies differential equation (II). Integration of equation (VII) yields the area under the curve for the tumor concentration $[L]_t$ as

$$AUC_t = \int_0^\infty [L]_t \, dt = \frac{1}{\rho + 1}\left(\rho\frac{1}{\kappa_f} + \frac{1}{\kappa_s}\right)\left[[L]_{t0} + \kappa_i\left(\frac{B_1}{\beta_1} + \frac{B_2}{\beta_2} + \frac{B_3}{\beta_3}\right)\right] \qquad (VIIa)$$

For simplicity, in the following, the parameters in equations (VI), (VIa), (VII), (VIIa) are assumed to comprise a general scaling factor and to be given in units of

– [%ID/g] for $[L]_t$, $[L]_{t0}$, $[L]_b$, B_1 , B_2 , B_3 ; and

– [%ID g^{-1} min] for AUC_b , AUC_t .

This assumption has no influence on key pharmacokinetic parameters, such as the rate constants κ_i , κ_f , κ_s and the dimensionless partition factor ρ . In addition, the use of a general scaling factor is common practice when dealing with TACs.

Equation (VII) formally corresponds to a sum of five exponential terms. If three exponential rate constants can be determined based on a blood TAC, the number of nominally adjustable parameters drops from ten to seven. The proposed PBPK model further reduces this number to four adjustable parameters. In a clinical setting the mass of the tumor compartment is small compared to healthy tissue. Accordingly, clearance from the tumor compartment has minor impact on the blood compartment. Under these "normal" conditions the blood compartment mainly exhibits renal and hepatobiliary excretion and to some extent radioligand recirculation due to clearance from healthy tissue. Contrary thereto, the blood TACs of Wang et al. are noticeably influenced by clearance from the abnormally large xenograft tumors. As consequence the triexponential fit to the blood TACs of Wang et al. involves at least one exponential term that mirrors tumor clearance.

Based on equation (VII) each of the four digitized tumor TACs of Wang et al. was fitted. The results are shown in Fig. 2 and Table 2. The fitted model curves generally agree well with the experimental data of Wang et al. as evidenced by the χ^2 values reported in Table 2. This suggests that the proposed PBPK model provides a fairly accurate description of experimental tumor TACs and can be used to extrapolate to times that exceed the measurement time of 180 minutes. However, this assumption needs to be confirmed by experiments over longer periods of time.

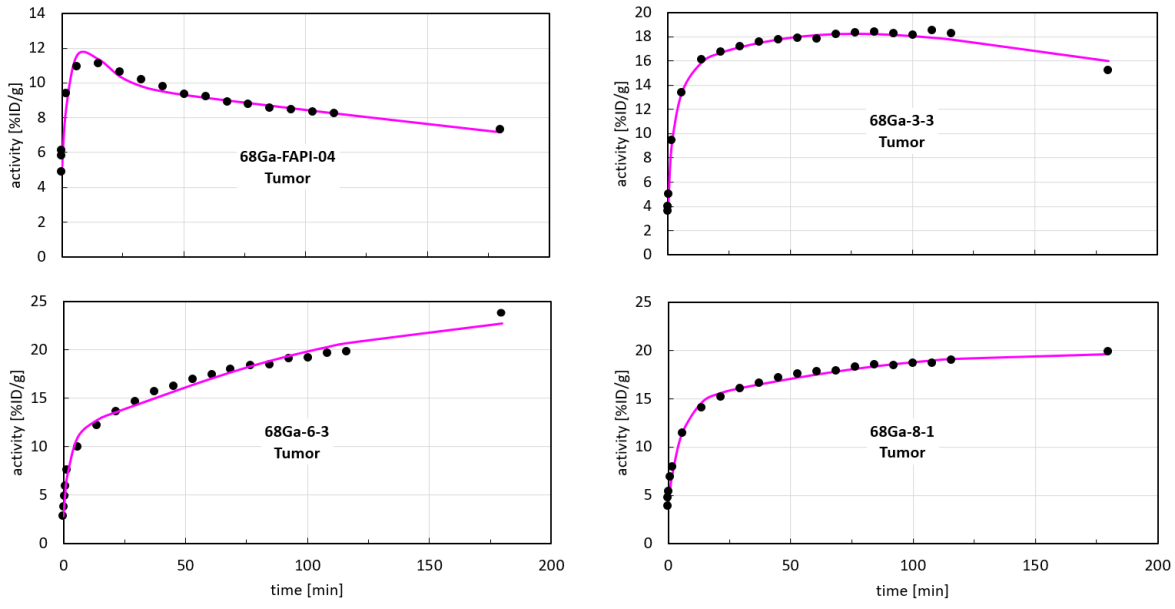

Fig. 2: Tumor TACs fitted to the data measured by Wang et al. [10].

	ρ	κ_i [min^{-1}]	κ_f [min^{-1}]	κ_s [min^{-1}]	$\sqrt{(\chi^2)}$ [%ID/g]	AUC_t [%ID g^{-1} min]	AUC_t / AUC_b
FAPI-04	10.30	0.30443	0.14298	0.00220	0.40	4859.3	14.9
Ga-3-3	1.19	0.45408	0.17705	0.01907	0.27	10188.4	12.4
Ga-6-3	2.87	0.27041	0.15377	0.00501	0.60	19204.3	15.5
Ga-8-1	3.45	0.16710	0.05505	0.00215	0.42	15767.2	20.6

Table 2: Fit parameters of the tumor TACs.

Despite the limitations mentioned above, the proposed PBPK model affords robust determination of model parameters κ_i, κ_f, κ_s, ρ and thereon based calculation of tumor dose (AUC_t) and tumor-to-blood dose ratio (AUC_t/AUC_b). It appears that the robustness of the proposed PBPK model is owed to the small number of adjustable parameters and that κ_i and ρ largely correspond to scaling factors with limited influence on the shape of the fitted TACs.

The proposed PBPK model can be advantageously used in the clinic, especially in settings where blood TACs are recorded simultaneously with dynamic PET, and may contribute to the understanding of pharmacokinetics and its impact on radioligand effectiveness.

As shown in Appendix B, a 5-compartment model cannot adequately describe the experimental results of Wang et al. This finding calls for caution when using a multi-compartment model and urges thorough analysis and comparison of the TACs and rate constants of all relevant tissues, with particular attention to liver and bone marrow. With this limitation in mind, the exponential rate constants derived by the proposed PBPK model are assumed to behave similarly to the eigenvalues $\lambda_{1\leq j\leq 5}$ of a 5-compartment model and represent bounds on the tissue rate constants.

The eigenvalues $\lambda_{1\leq j\leq N}$ of a general N-compartment model are complicated functions of the underlying tissue uptake and clearance rate constants $k_{1\leq i\leq 2N-1}$. For given tissue rate constants $k_{1\leq i\leq 2N-1}$, the eigenvalues $\lambda_{1\leq j\leq N}$ satisfy the condition

$$\min_{1\leq j\leq N}\left|\lambda_j\right| \leq k_{1\leq i\leq 2N-1} \leq \max_{1\leq j\leq N}\left|\lambda_j\right| \qquad (VIII)$$

FAP radioligands are excreted from the central blood compartment via the renal or hepatobiliary pathway either directly or after tissue perfusion and reentry, i.e. clearance into the blood compartment. Accordingly, the blood and tumor TACs are complex functions of tissue clearance and systemic excretion.

Hydrophilic radioligands tend to have high tissue diffusivity and are preferably excreted via the kidneys. Conversely, lipophilic radioligands perfuse slowly and are more likely to be excreted via the hepatobiliary pathway.

Heuristically, blood and tissue TACs are expected to comprise a ligand or activity component that has traveled a maximal path between injection and systemic excretion. However, depending on the amount of this component it may not noticeably contribute to either the blood or tumor TAC.

Based on this reasoning, the larger of the exponential rate constants β_3 and κ_s reported in Table 1 and Table 2 is considered as approximation $\tilde{\kappa}_e$ for the effective tumor clearance rate κ_e, i.e. $\tilde{\kappa}_e = \max\{\beta_3, \kappa_s\}$. If κ_{PK} and K_D are known, $\tilde{\kappa}_e$ can be substituted into equation (I) to estimate the intratumoral receptor concentration $[R]_t$ according to the formula

$$[R]_t \approx \left(\frac{\kappa_{PK}}{\tilde{\kappa}_e} - 1\right) K_D \qquad (Ia)$$

Table 3 lists logP, IC_{50}, $\tilde{\kappa}_e$ and corresponding binding half-lives $\frac{\ln 2}{\tilde{\kappa}_e}$ for radioligands FAPI-04, Ga-3-3, Ga-6-3, Ga-8-1.

Radioligand	***logP****	***IC_{50} [nM]***	***$\tilde{\kappa}_e$ [min^{-1}]***	***$\frac{ln\,2}{\tilde{\kappa}_e}$ [min]***
Ga-3-3	-3.23	2.2	0.019071	36.3
FAPI-04	-2.42	3.8	0.013870	50.0
Ga-8-1	-2.55	3.3	0.005725	121.1
Ga-6-3	-1.51	1.9	0.005007	138.4

*Table 3: Radioligand pharmacokinetic parameters (*logP for FAPI-04 adopted from Yang et al., page 2334, right column, 1st paragraph [4]).*

The above data does not exhibit a systematic correlation between logP or IC_{50} and the binding half-life $\frac{\ln 2}{\tilde{\kappa}_e}$. Obviously, though, the naphthol moiety (cf. Fig. 3) incorporated in Ga-6-3 and Ga-8-1 substantially prolongs the binding half-life $\frac{\ln 2}{\tilde{\kappa}_e}$ relative to FAPI-04 and Ga-3-3. It appears that the prolongation imparted by naphthol is attributable to increased lipophilicity and protein affinity. Surprisingly, the latter does not seem to be FAP specific.

The rather high IC_{50} value of Ga-8-1 and the strong uptake of Ga-6-3 in liver tissue point to a nonspecific pharmacokinetic mechanism.

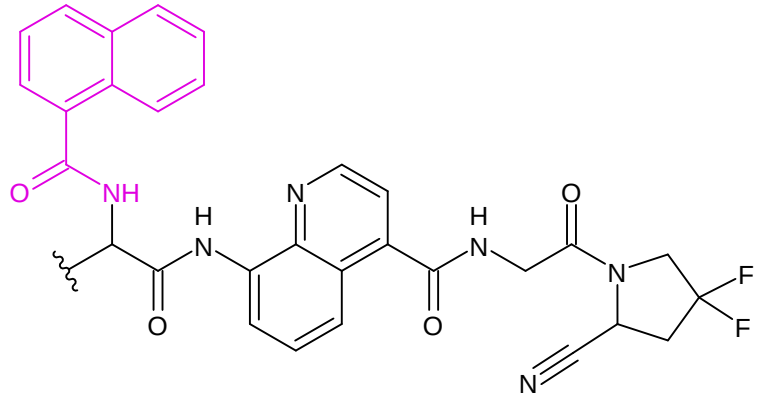

Fig. 3: Naphthol moiety (marked in magenta) incorporated in radioligands Ga-6-3 and Ga-8-1 [10].

As discussed in Appendix B, the authors attempted to reproduce the tumor TACs of Wang et al. based on a 5-compartment model with nine adjustable rate constants. For radioligands Ga-3-3, Ga-6-3 and Ga-8-1 it was not possible to fit the experimental data in a satisfactory manner. It appears, that despite large degrees of freedom, a 5-compartment model cannot adequately describe the particular pharmacokinetics of these radioligands.

References

1. Jagannathan K, Gupta AK, Nguyen TT. Skewed Double Exponential Distribution and Its Stochastic Representation. European Journal of Pure and Applied Mathematics [Internet]. 2009; 2:[1-20 pp.]. Available from: https://ejpam.com/index.php/ejpam/article/view/390.

2. Wen X, Xu P, Zeng X, Liu J, Du C, Zeng X, et al. Development of [177Lu]Lu-LNC1003 for radioligand therapy of prostate cancer with a moderate level of PSMA expression. European Journal of Nuclear Medicine and Molecular Imaging 2023 50:9 [Internet]. 2023-04-25; 50(9). Available from: https://link.springer.com/article/10.1007/s00259-023-06229-w.

3. Galler M, Chibolela C, Rogasch JMM, Huang K, Siefert J, Schatka I, et al. Dosimetric analysis of a compartmental model for radioligand uptake in tumor lesions. Biomedical Physics & Engineering Express [Internet]. 2023-07-19; 9(5). Available from: https://iopscience.iop.org/article/10.1088/2057-1976/ace44a.

4. Yang T, Peng L, Qiu J, He X, Zhang D, Wu R, et al. A radiohybrid theranostics ligand labeled with fluorine-18 and lutetium-177 for fibroblast activation protein-targeted imaging and radionuclide therapy. European Journal of Nuclear Medicine and Molecular Imaging 2023 50:8 [Internet]. 2023-03-03; 50(8). Available from: https://link.springer.com/article/10.1007/s00259-023-06169-5.

5. Millul J, Bassi G, Mock J, Elsayed A, Pellegrino C, Zana A, et al. An ultra-high-affinity small organic ligand of fibroblast activation protein for tumor-targeting applications. Proc Natl Acad Sci U S A [Internet]. 2021 Apr 20 PMC8072232]; 118(16). Available from: https://pubmed.ncbi.nlm.nih.gov/33850024/.

6. Lin J-J, Chuang C-P, Lin J-Y, Huang F-T, Huang C-W. Rational Design, Pharmacomodulation, and Synthesis of [68Ga]Ga-Alb-FAPtp-01, a Selective Tumor-Associated Fibroblast Activation Protein Tracer for PET Imaging of Glioma. ACS Sensors [Internet]. 2021 2021/09/24; 6(9):[3424-35 pp.]. Available from: https://doi.org/10.1021/acssensors.1c01316.

7. Younis MH, Malih S, Lan X, Rasaee MJ, Cai W. Enhancing fibroblast activation protein (FAP)-targeted radionuclide therapy with albumin binding, and beyond. European Journal of Nuclear Medicine and Molecular Imaging [Internet]. 2022 2022-05-01; 49(6):[1773-7 pp.]. Available from: https://link.springer.com/article/10.1007/s00259-022-05766-0.

8. Kuo H-T, Lin K-S, Zhang Z, Uribe CF, Merkens H, Zhang C, et al. ¹⁷⁷Lu-Labeled Albumin-Binder–Conjugated PSMA-Targeting Agents with Extremely High Tumor Uptake and Enhanced Tumor-to-Kidney Absorbed Dose Ratio. Journal of Nuclear Medicine [Internet]. 2021 2021-04-01; 62(4):[521-7 pp.]. Available from: https://pubmed.ncbi.nlm.nih.gov/32859704/.

9. Lindeman SD, Mukkamala R, Horner A, Tudi P, Booth OC, Huff R, et al. Fibroblast Activation Protein–Targeted Radioligand Therapy for Treatment of Solid Tumors. Journal of Nuclear Medicine [Internet]. 2023 2023-05-01; 64(5):[759-66 pp.]. Available from: https://pubmed.ncbi.nlm.nih.gov/37116911/.

10. Wang Y, Yuan H, Liu N, Tang S, Feng Y, Liu Y, et al. High Affinity and FAP-Targeted Radiotracers: A Potential Design Strategy to Improve the Pharmacokinetics and Tumor Uptake for FAP Inhibitors. Journal of Medicinal Chemistry [Internet]. 2023 2023/07/13; 66(13):[8614-27 pp.]. Available from: https://doi.org/10.1021/acs.jmedchem.3c00259.

11. Zhang H, Yue X, Chen Z, Liu C, Wu W, Zhang N, et al. Define cancer-associated fibroblasts (CAFs) in the tumor microenvironment: new opportunities in cancer immunotherapy and advances in clinical trials. Molecular Cancer [Internet]. 2023 2023-10-02; 22(1). Available from: https://molecular-cancer.biomedcentral.com/articles/10.1186/s12943-023-01860-5.

12. Ballal S, Yadav MP, Moon ES, Kramer VS, Roesch F, Kumari S, et al. First-In-Human Results on the Biodistribution, Pharmacokinetics, and Dosimetry of [177Lu]Lu-DOTA.SA.FAPi and [177Lu]Lu-DOTAGA.(SA.FAPi)2. Pharmaceuticals [Internet]. 2021 2021-11-24; 14(12):[1212 p.]. Available from: https://www.mdpi.com/1424-8247/14/12/1212.

13. Ballal S, Yadav MP, Moon ES, Rösch F, ArunRaj ST, Agarwal S, et al. First-in-Human Experience With 177Lu-DOTAGA.(SA.FAPi)2 Therapy in an Uncommon Case of Aggressive Medullary Thyroid Carcinoma Clinically Mimicking as Anaplastic Thyroid Cancer. Clin Nucl Med [Internet]. 2022 Jun 1; 47(6):[e444-e5 pp.]. Available from: https://pubmed.ncbi.nlm.nih.gov/35507435/.

14. Ballal S, Yadav MP, Raju S, Roesch F, Martin M, Tripathi M, et al. [177Lu]Lu-DOTAGA.Glu.(FAPi)2 Radionuclide Therapy: a New Treatment Option for Patients with Glioblastoma Multiforme. Nuclear Medicine and Molecular Imaging [Internet]. 2023 2023-07-14. Available from: https://pubmed.ncbi.nlm.nih.gov/38261876/.

15. Wikipedia: Runge-Kutta methods [Available from: https://en.wikipedia.org/wiki/Runge%E2%80%93Kutta_methods.

Appendix A

In thermal equilibrium, the same number of complexes RL are formed and dissociate in every unit of time and volume. The number of newly formed and dissociating complexes per unit of time and volume is proportional to the receptor concentration $[R]$ and the ligand concentration $[L]$ with the proportionality constant $\mathrm{k_{on}}$ and proportional to the complex concentration $[RL]$ with the proportionality constant $\mathrm{k_{off}}$, respectively.

$$\frac{d[RL]}{dt} = \mathrm{k_{on}} \cdot [R] \cdot [L] - \mathrm{k_{off}} \cdot [RL] = 0 \qquad (A1)$$

Accordingly, we get

$$\mathrm{k_{on}} \cdot [R] \cdot [L] = \mathrm{k_{off}} \cdot [RL] \qquad (A2)$$

and

$$\frac{[R] \cdot [L]}{[RL]} = \frac{\mathrm{k_{off}}}{\mathrm{k_{on}}} = K_D \qquad (A3)$$

with the dissociation constant K_D (or reciprocal of the affinity). Transforming equation (A3) yields:

$$[L] = \frac{K_D}{K_D + [R]} ([L] + [RL]) \qquad (A3)$$

Radioligand clearance from tumor tissue is proportional to the concentration $[L]$ of unbound radioligand and the "regular" pharmacokinetic clearance rate k_{PK} without receptor interference

$$\frac{d}{dt}([L] + [RL]) = -k_{PK} \cdot [L] = -k_{PK} \frac{K_D}{K_D + [R]} ([L] + [RL]) \qquad (A4)$$

This gives us the effective clearance rate

$$k_e = k_{PK} \frac{K_D}{K_D + [R]} \qquad (A5)$$

According to equation (A5), $k_e < k_{PK}$ for all values of K_D and $[R]$. For low affinity, i.e. $K_D \gg [R]$, k_e tends toward k_{PK} ($k_e \to k_{PK}$). Conversely, for very high affinity $K_D \to 0$, k_e tends toward 0 ($k_e \to 0$).

A typical scenario with K_D = 4.7 nM and $[R]$ = 16 nM yields $\frac{K_D}{K_D+[R]}$ = 0.23, i.e. the effective tumor clearance rate k_e is smaller (slower) by a factor of 4.4 relative to the "regular" pharmacokinetic clearance rate k_{PK}. For fixed K_D and $[R]$ the effective clearance rate k_e can be altered by changing the pharmacokinetic clearance rate k_{PK}. Generally, a modification of radioligand chemistry affects both K_D and k_{PK}.

For therapeutically effective radioligand retention in tumor tissue a 1:10 ratio according to the formula

$$K_D \leq 0.1 \cdot [R] \qquad (A6)$$

can serve as rule of thumb.

Appendix B

PBPK models for RLT are usually based on a multi-compartment model and respective system of coupled linear differential equations.

The PBPK model proposed in this article is based on equation (VII) which formally corresponds to a sum of five exponential functions. Hence, the authors sought to construct an analogous 5-compartment model.

For this purpose, three different 5-compartment models with characteristic matrices $\widetilde{M}_1$, $\widetilde{M}_2$, $\widetilde{M}_3$ were examined.

$$\widetilde{M}_1 = \begin{pmatrix} K & k_{1b} & k_{2b} & k_{3b} & k_{4b} \\ k_{b1} & -k_{1b} & 0 & 0 & 0 \\ k_{b2} & 0 & -k_{2b} & 0 & 0 \\ k_{b3} & 0 & 0 & -k_{3b} & 0 \\ k_{b4} & 0 & 0 & 0 & -k_{4b} \end{pmatrix} \qquad \widetilde{M}_2 = \begin{pmatrix} K & 0 & 0 & 0 & 0 \\ k_{b1} & -k_{1b} & 0 & 0 & 0 \\ k_{b2} & 0 & -k_{2b} & 0 & 0 \\ k_{b3} & 0 & 0 & -k_{3b} & 0 \\ k_{b4} & 0 & 0 & 0 & -k_{4b} \end{pmatrix}$$

$$K = -k_{be} - k_{b1} - k_{b2} - k_{b3} - k_{b4}$$

$\widetilde{M}_1$ and $\widetilde{M}_2$ represent models with one blood and four tissue compartments with corresponding rate constants k_{be} , k_{1b} , k_{2b} , k_{3b} , k_{4b} for blood excretion and tissue clearance, and k_{b1} , k_{b2} , k_{b3} , k_{b4} for tissue uptake. $\widetilde{M}_2$ differs from $\widetilde{M}_1$ in that recirculation from the four tissue compartments into the blood compartment is neglected.

$$\widetilde{M}_3 = \begin{pmatrix} K' & k_{va} & 0 & 0 & 0 \\ k_{av} & -k_{va} & k_{1v} & k_{2v} & k_{3v} \\ k_{a1} & 0 & -k_{1v} & 0 & 0 \\ k_{a2} & 0 & 0 & -k_{2v} & 0 \\ k_{a3} & 0 & 0 & 0 & -k_{3v} \end{pmatrix}$$

$$K' = -k_{ae} - k_{a1} - k_{a2} - k_{a3} - k_{av}$$

$\widetilde{M}_3$ corresponds to a model with two compartments for arterial and venous blood and three tissue compartments. Therein k_{ae} , k_{av} , k_{va} are the rate constants for arterial excretion and arterial-venous recirculation, whereas k_{a1} , k_{a2} , k_{a3} , k_{1v} , k_{2v} , k_{3v} denote rates for tissue uptake from arterial blood and clearance into venous blood, respectively.

The rate constants or coefficients of each of matrices $\widetilde{M}_1$, $\widetilde{M}_2$, $\widetilde{M}_3$ were fitted to the tumor TAC of each of radioligands FAPI-04, Ga-3-3, Ga-6-3 and Ga-8-1 using a Nelder-Mead optimization algorithm (https://en.wikipedia.org/wiki/Nelder-Mead_method). The corresponding blood TACs were not included in order to alleviate the optimization restraints.

The rate constants or coefficients of each of matrices $\widetilde{M}_1$, $\widetilde{M}_2$, $\widetilde{M}_3$ are equivalent to the rate constants of a system of five coupled differential equations. Rather than using numerical integration based on a Runge-Kutta method [15], the five eigenvalues and eigenvectors

$\{\lambda_j, \vec{e}_j \mid j = 1,2,3,4,5\}$ of the matrices $\widetilde{M}_1, \widetilde{M}_2, \widetilde{M}_3$ were numerically determined in each iteration of the optimization procedure. A linear superposition according to formula (IB)

$$\sum_{j=1}^{5} c_j \left(\vec{e}_j \, e^{\lambda_j t}\right) \qquad (IB)$$

with five coefficients $\{c_j \mid j = 1,2,3,4,5\}$ constitutes a solution to the system of coupled differential equations. The coefficients c_j are determined by solving the linear system of equations for the boundary conditions at time t = 0.

The eigenvalue approach avoids the instabilities that frequently plague the numerical integration of "stiff" differential equation systems with rate constants that differ by two or three orders of magnitude.

For the first model with characteristic matrix $\widetilde{M}_1$ the results of the optimization procedure are presented in Table B 1 and Fig. B 1. While it was possible to match the tumor TACs of FAPI-04 and Ga-8-1 with satisfactory conformance the agreement for Ga-3-3 and Ga-6-3 is poor, despite exclusion of the blood TACs and the rather large degrees of freedom. Moreover, for Ga-3-3, Ga-6-3 and Ga-8-1 the resultant rate constant for tumor clearance tends towards zero, i.e. infinite retention, which obviously contradicts experimental results obtained by Wang et al. and others.

For the second and third model with matrix $\widetilde{M}_2$ and $\widetilde{M}_3$ similar problems were observed. These findings suggest that standard 5-compartment models are not suitable to reflect the particular pharmacokinetic processes that underlie the experimental data of Wang et al.

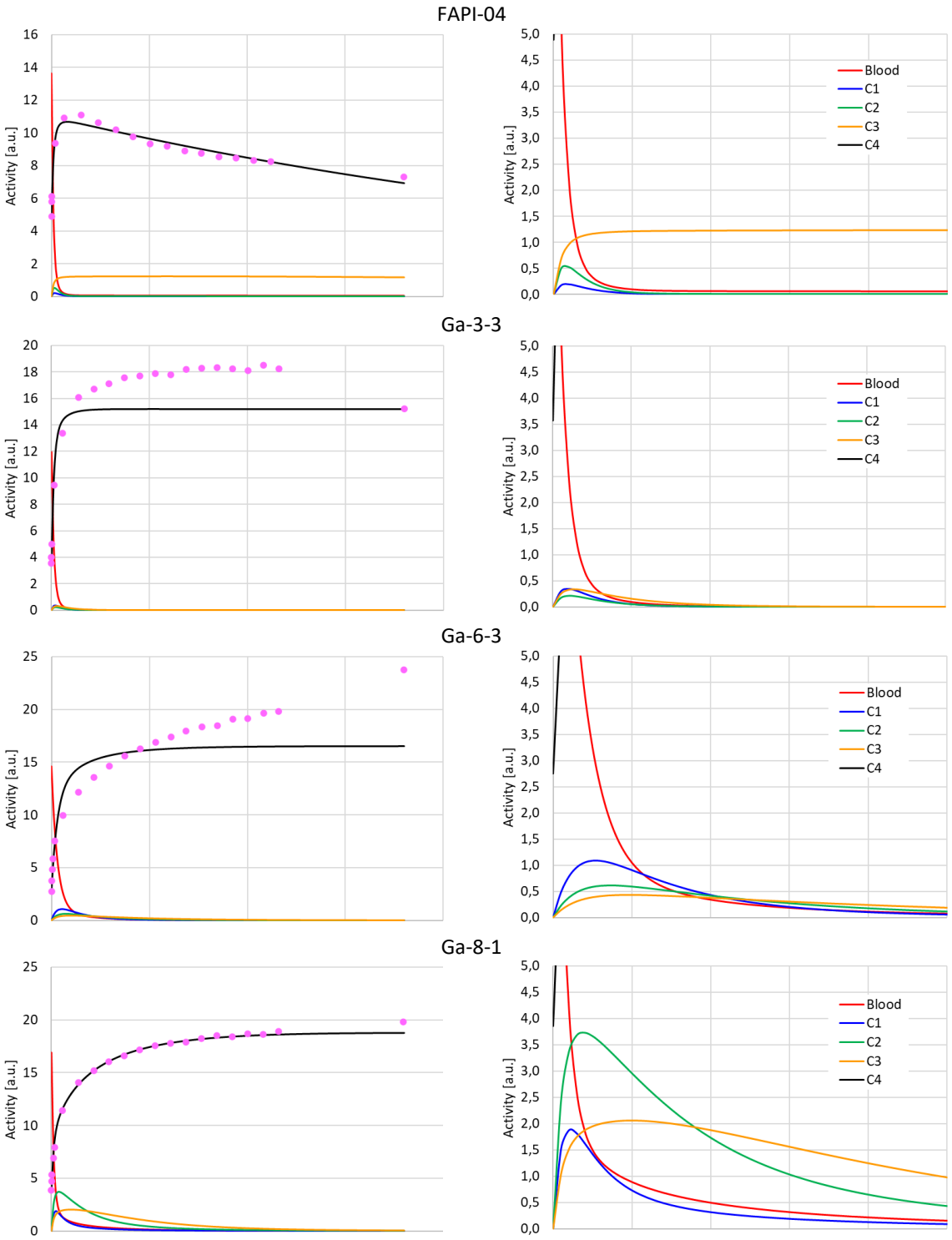

Fig. B 1: Blood and tumor TACs of the optimized 5-compartment model based on the data measured by Wang et al. [10]

FAPI-04

k_{be}	0,42006177					
k_{1b} , k_{2b} , k_{3b} , k_{4b}	0,37882609	0,45581095	0,00383740	0,00509612		
k_{b1} , k_{b2} , k_{b3} , k_{b4}	0,02587164	0,07576694	0,08158189	0,40980672		
λ_b , λ_1 , λ_2 , λ_3 , λ_4	-1,08417046	-0,41596971	-0,35022882	-0,00410030	-0,00219022	
c_{bb} , c_{b1} , c_{b2} , c_{b3} , c_{b4}	12,25707814	0,45383519	0,84128534	0,00582191	0,06097942	
c_{1b} , c_{11} , c_{12} , c_{13} , c_{14}	-0,44958276	-0,31610971	0,76110175	0,00040195	0,00418876	
c_{2b} , c_{21} , c_{22} , c_{23} , c_{24}	-1,47794571	0,86306804	0,60371593	0,00097653	0,01018521	
c_{3b} , c_{31} , c_{32} , c_{33} , c_{34}	-0,92559941	-0,08983701	-0,19813900	-1,80663161	3,02020703	$\sqrt{(\chi^2)}$
c_{4b} , c_{41} , c_{42} , c_{43} , c_{44}	-4,65494620	-0,45265677	-0,99893282	2,39586683	8,59966897	**0,33**

Ga-3-3

k_{be}	0,01916959					
k_{1b} , k_{2b} , k_{3b} , k_{4b}	0,34516116	0,26298032	0,15272322	0,00021622		
k_{b1} , k_{b2} , k_{b3} , k_{b4}	0,04445203	0,02453410	0,03317489	0,69473395		
λ_b , λ_1 , λ_2 , λ_3 , λ_4	-0,86369475	-0,32106156	-0,24897878	-0,14340459	-0,00000580	
c_{bb} , c_{b1} , c_{b2} , c_{b3} , c_{b4}	11,01221836	0,40489350	0,33079422	0,19849340	0,00460051	
c_{1b} , c_{11} , c_{12} , c_{13} , c_{14}	-0,94403811	0,74683138	0,15288116	0,04373307	0,00059249	
c_{2b} , c_{21} , c_{22} , c_{23} , c_{24}	-0,44975594	-0,17103110	0,57963170	0,04072613	0,00042920	
c_{3b} , c_{31} , c_{32} , c_{33} , c_{34}	-0,51384499	-0,07979346	-0,11400965	0,70664873	0,00099937	$\sqrt{(\chi^2)}$
c_{4b} , c_{41} , c_{42} , c_{43} , c_{44}	-8,86016462	-0,87672540	-0,92382864	-0,96306777	15,18978642	**2,28**

Ga-6-3

k_{be}	0,01285646					
k_{1b} , k_{2b} , k_{3b} , k_{4b}	0,11015915	0,05620284	0,02992909	0,00019661		
k_{b1} , k_{b2} , k_{b3} , k_{b4}	0,04085516	0,01903479	0,01169943	0,23716418		
λ_b , λ_1 , λ_2 , λ_3 , λ_4	-0,34566051	-0,09308429	-0,05114738	-0,02819543	-0,00001009	
c_{bb} , c_{b1} , c_{b2} , c_{b3} , c_{b4}	13,28854644	0,84222053	0,32437035	0,12183425	0,01302843	
c_{1b} , c_{11} , c_{12} , c_{13} , c_{14}	-2,30531841	2,01518848	0,22456880	0,06072879	0,00483235	
c_{2b} , c_{21} , c_{22} , c_{23} , c_{24}	-0,87385720	-0,43467623	1,22131747	0,08280270	0,00441326	
c_{3b} , c_{31} , c_{32} , c_{33} , c_{34}	-0,49240722	-0,15602042	-0,17885270	0,82218575	0,00509459	$\sqrt{(\chi^2)}$
c_{4b} , c_{41} , c_{42} , c_{43} , c_{44}	-9,12271070	-2,15038792	-1,50986982	-1,03199790	16,56596634	**2,33**

Ga-8-1

k_{be}	0,03711453					
k_{1b} , k_{2b} , k_{3b} , k_{4b}	0,30251036	0,11734788	0,03929789	0,00016964		
k_{b1} , k_{b2} , k_{b3} , k_{b4}	0,15308706	0,22169987	0,09084287	0,30280958		
λ_b , λ_1 , λ_2 , λ_3 , λ_4	-0,91749277	-0,24357421	-0,07568756	-0,02810666	-0,00001848	
c_{bb} , c_{b1} , c_{b2} , c_{b3} , c_{b4}	14,46366478	1,05210959	0,86157135	0,50424105	0,00941323	
c_{1b} , c_{11} , c_{12} , c_{13} , c_{14}	-3,60042814	2,73286213	0,58149108	0,28131102	0,00476391	
c_{2b} , c_{21} , c_{22} , c_{23} , c_{24}	-4,00751493	-1,84789149	4,58494532	1,25267431	0,01778678	
c_{3b} , c_{31} , c_{32} , c_{33} , c_{34}	-1,49616094	-0,46787930	-2,15081966	4,09308959	0,02177031	$\sqrt{(\chi^2)}$
c_{4b} , c_{41} , c_{42} , c_{43} , c_{44}	-4,77447487	-1,30888613	-3,45470371	-5,46547147	18,85653618	**0,37**

Table B 1: Coefficients of the optimized 5-compartment model.